JOURNAL OF SPACECRAFT AND ROCKETS
Vol. 40, No. 3, May–June 2003

Computational Aerothermodynamics in Aeroassist Applications

Peter A. Gnoffo*
NASA Langley Research Center, Hampton, Virginia 23681-0001

Aeroassisted planetary entry uses atmospheric drag to decelerate spacecraft from superorbital to orbital or suborbital velocities. Numerical simulation of flowfields surrounding these spacecraft during hypersonic atmospheric entry is required to define aerothermal loads. The severe compression in the shock layer in front of the vehicle and subsequent, rapid expansion into the wake are characterized by high-temperature, thermochemical nonequilibrium processes. Implicit algorithms required for efficient, stable computation of the governing equations involving disparate timescales of convection, diffusion, chemical reactions, and thermal relaxation are discussed. Robust point-implicit strategies are utilized in the initialization phase; less robust, but more efficient line-implicit strategies are applied in the endgame. Applications to ballutes (balloonlike decelerators) in the atmospheres of Venus, Mars, Titan, Saturn, and Neptune and a Mars Sample Return Orbiter are featured. Examples are discussed where time-accurate simulation is required to achieve a steady-state solution.

Nomenclature

A_L	=	$\partial \bar{\boldsymbol{r}}_L / \partial \bar{\boldsymbol{q}}_{L-1}$; Eq. (5a)
A_m	=	$(\partial \bar{\boldsymbol{f}}_m / \partial \bar{\boldsymbol{q}}_m)\sigma_m$
B_L	=	$\partial \bar{\boldsymbol{r}}_L / \partial \bar{\boldsymbol{q}}_L$; Eq. (1)
B_m	=	$-(\partial \bar{\boldsymbol{h}}_m / \partial \Delta \bar{\boldsymbol{q}})(\partial \Delta \bar{\boldsymbol{q}} / \partial \bar{\boldsymbol{q}}_L)\sigma_m$
C_L	=	$\partial \bar{\boldsymbol{r}}_L / \partial \bar{\boldsymbol{q}}_{L+1}$; Eq. (5b)
c_1, c_2	=	inviscid and viscous relaxation factors, respectively
D	=	diameter, m
$\bar{\boldsymbol{f}}$	=	inviscid flux vector
$\bar{\boldsymbol{h}}$	=	viscous flux vector
L	=	cell index or reference length, m
M	=	Mach number
M_L	=	inviscid flux part of B_L; Eq. (2)
N_L	=	viscous flux part of B_L; Eq. (3)
p	=	pressure, N/m^2
$\boldsymbol{q}$	=	dependent variable vector
q_w	=	wall heat transfer rate, W/cm^2
Re	=	Reynolds number
$\bar{\boldsymbol{r}}_L$	=	residual vector at cell L
S_L	=	source term part of B_L
T	=	translational–rotational temperature, K
T_V	=	vibrational–electronic temperature, K
V_∞	=	freestream velocity, m/s
x, y, z	=	Cartesian coordinates, m
λ	=	eigenvalue
ρ	=	density, kg/m^3
σ	=	cell wall area, m^2
χ_i	=	mole fraction of species i
Ω	=	cell volume, m^3

Subscripts

i	=	species index
m	=	cell wall index
w	=	wall surface conditions
∞	=	freestream conditions

Presented as Paper 2001-2632 at the AIAA 15th Computational Fluid Dynamics Conference, Anaheim, CA, 11–14 June 2001; received 20 July 2001; revision received 25 May 2002; accepted for publication 3 June 2002.

*Senior Research Engineer, Aerothermodynamics Branch, Mail Stop 408A; p.a.gnoffo@larc.nasa.gov. Associate Fellow AIAA.

Introduction

AEROASSISTED planetary entry uses atmospheric drag to decelerate spacecraft from superorbital to orbital or suborbital velocities. The vehicles encounter flow domains from free-molecular to continuum.[1] The severe compression in the shock layer in front of the vehicle and subsequent, rapid expansion into the wake are characterized by high-temperature, thermochemical nonequilibrium processes. The chemical state of atmospheric constituents crossing the bow shock varies from frozen to nonequilibrium (ionization, dissociation) to equilibrium. The thermal state of internal energy modes (electronic, vibrational, rotational) varies similarly. Convective heating rates are strongly influenced by the catalytic properties of the surface and diffusion rate of atoms to the wall.

Numerical simulations are the primary source for defining environments and vehicle response to environments required in the design of planetary entry vehicles. The simulations are verified when possible with ground-based and flight-test data that cover some subset of the entry corridor parameter space. Implicit algorithms are required for efficient, stable computation of the governing equations involving the disparate timescales of convection, diffusion, chemical reactions, and thermal relaxation. Point- and line-implicit treatments provide opportunities for single-level storage relaxation at the expense of time accuracy. The essence of a point-implicit method is to treat all contributions to the residual from the cell center at the advanced time level; upwind formulations enable this structure by introducing cell center dependence from the convective terms. Implicit lines running across the viscous layer, solved by block tridiagonal relaxation, utilize the same Jacobian blocks from the point-implicit formulation in the center diagonal, but provide enhanced convergence.

This paper reviews these implicit algorithms as applied in the algorithm LAURA[2] to a variety of challenging (from perspective of physical and geometric complexity) problems in aeroassist simulation. An interesting outcome of this review is the identification of hypersonic flow geometries in which attainment of a steady-state solution requires a time-accurate simulation; constant Courant number simulations lead to nonphysical, unsteady flow.

Algorithm

Point-Implicit Relaxation

LAURA employs two relaxation modes: point-implicit and line-implicit. The point-implicit mode[2,3] implicitly solves only contributions of dependent variables at cell L, $\bar{\boldsymbol{q}}_L$, to the residual at cell L, $\bar{\boldsymbol{r}}_L$; contributions from dependent variables at neighbor cells are treated explicitly. The contributions of inviscid, viscous, and source terms are included in the point-implicit matrix B_L, as follows:

$$B_L = S_L \Omega_L + c_1 M_L + c_2 N_L \tag{1}$$

where S_L is the Jacobian of the chemical and thermal source term components of the residual, M_L is the Jacobian of the inviscid terms,

and N_L is the Jacobian of the viscous terms, all with respect to $\bar{q}_L$. Scalar constants $c_1 > 1.5$ and $c_2 > 0.5$ are relaxation factors. Typical values are $c_1 = 3$ and $c_2 = 1$. Relaxation factors on the source term Jacobian have never been required.

Within the context of flux difference splitting (FDS) and Roe's averaging[4] the inviscid Jacobian is defined as

$$M_L = \frac{1}{2}\sum_m |A_m|\sigma_m \tag{2}$$

where m is summed over all faces of cell L, A_m is Roe's averaged flux Jacobian at face m, and $|A_m|$ is defined using the absolute values of the eigenvalues of A_m. The elements of A_m are required in the definition of the FDS formulation of the inviscid flux; consequently, it is economical to reuse these quantities in the formulation of the Jacobian. The absolute value of the eigenvalues may be limited from below using a variation of Harten's entropy fix[5] (also see Ref. 3). This limiter serves to enhance stability of the relaxation algorithm and prevent formation of expansion shocks across sonic lines or carbuncles in the stagnation region.

The viscous Jacobian is defined as

$$N_L = \sum_m B_m \sigma_m \tag{3}$$

where B_m is the Jacobian of viscous terms across the mth face of cell L. It implicitly treats only the divided difference across the cell face. Transport properties at cell face m are linear averages of adjacent cell center values. Velocities in the shear work term are the Roe-averaged quantities already computed for the inviscid flux function. Eigenvalues of B_m are positive or zero.

The change in dependent variables after a single, point-implicit relaxation step is computed as follows:

$$[(\Omega_L/\Delta t_L)I + B_L]\Delta\bar{q}_L = \bar{r}_L \tag{4}$$

where I, the identity matrix; Ω_L, the volume; and Δt_L, the time step at cell L (often derived from a constant Courant number specification) are associated with the time derivative term of the conservation equations. In cases with crudely defined initial conditions or with difficult transients, stability is maintained by temporarily increasing the relaxation factors c_1 and c_2. Values of 10 are usually sufficient; values up to 100 have been required on some highly energetic, multispecies aeroassist simulations.

Line-Implicit Relaxation

The point-implicit option is not efficient for relaxing the viscous layers. Some efficiency can be recovered by using multitasking with majority of cycles in the boundary layer or by using an overrelaxation factor $1 > c_2 > 0.5$. However, a better approach is to introduce implicit dependence of the solution across the entire shock layer.

The line-implicit[6] relaxation algorithm is a simple extension of the point-implicit algorithm. However, approximations to A_L, the Jacobian of $\bar{r}_L$ with respect to $\bar{q}_{L-1}$, and C_L, the Jacobian of $\bar{r}_L$ with respect to $\bar{q}_{L+1}$, are introduced to preserve symmetry of form with B_L that also improves convergence. They are defined as

$$A_L = \begin{bmatrix} -(c_1/2)\left(\left|A_{L-\frac{1}{2}}\right| + A_{L-\frac{1}{2}}\right) \\ -c_2 B_{L-\frac{1}{2}} \end{bmatrix} \sigma_{L-\frac{1}{2}} \tag{5a}$$

$$C_L = \begin{bmatrix} -(c_1/2)\left(\left|A_{L+\frac{1}{2}}\right| - A_{L+\frac{1}{2}}\right) \\ -c_2 B_{L+\frac{1}{2}} \end{bmatrix} \sigma_{L+\frac{1}{2}} \tag{5b}$$

It is assumed that sequential indices L define a continuous series of cells spanning some portion of the computational domain. The subscripts $L \pm \frac{1}{2}$ refer to Roe-averaged conditions on face m between cell centers L and $L \pm 1$, respectively. A more exact linearization of the residual would lead to use of $A_{L\pm1}$ in place of $A_{L\pm1/2}$ in the second occurrence of Eqs. (5); however, the present formulation provides exact cancellation of convective, downwind implicit influences and exhibits more robust convergence characteristics, particularly in the vicinity of strong shock waves at large Courant numbers.

In the present work, the source term requires no off-diagonal, implicit contribution. The line-implicit relaxation in Eq. (6) requires approximately 2.8 times more CPU time per iteration as the point-implicit algorithm in the applications described here, but the convergence rate more than makes up for this overhead. It requires additional storage for the off-diagonal blocks:

$$\begin{bmatrix} B_L & C_L & 0 & 0 & 0 \\ A_{L+1} & B_{L+1} & C_{L+1} & 0 & 0 \\ 0 & \ddots & \ddots & \ddots & 0 \\ 0 & 0 & A_{L+N-1} & B_{L+N-1} & C_{L+N-1} \\ 0 & 0 & 0 & A_{L+N} & B_{L+N} \end{bmatrix} \cdot \begin{bmatrix} \Delta\bar{q}_L \\ \Delta\bar{q}_{L+1} \\ \vdots \\ \Delta\bar{q}_{L+N-1} \\ \Delta\bar{q}_{L+N} \end{bmatrix} = \begin{bmatrix} \bar{r}_L \\ \bar{r}_{L+1} \\ \vdots \\ \bar{r}_{L+N-1} \\ \bar{r}_{L+N} \end{bmatrix} \tag{6}$$

Implicit Boundary Conditions

Implicit treatment of boundary conditions is required to obtain good convergence with line relaxation. Boundary conditions in the present formulation are implemented with ghost cells. If the off-diagonal Jacobian at the ghost cell for $L = 1$ is A_0, then B_1 is augmented by $A_0 W_0^{-1} W_1$, where

$$W_0\, \mathrm{d}\bar{q}_0 = W_1\, \mathrm{d}\bar{q}_1 \tag{7}$$

is an expression of the dependence of the ghost cell on the boundary cell. In like manner, B_N is augmented by $C_{N+1} W_{N+1}^{-1} W_N$, where $\boldsymbol{W}_{N+1}\, \mathrm{d}\bar{\boldsymbol{q}}_{N+1} = \boldsymbol{W}_N\, \mathrm{d}\bar{\boldsymbol{q}}_N$.

Time Accuracy

The LAURA algorithm, in its default mode, uses single-level storage and relaxes the steady form of the governing equations with a Courant number of 10^6. However, some applications considered here require time-accurate relaxation. Time accuracy (first order in Δt) can be recovered by using constant time-step advancement at all cells and by employing two levels of storage with subiterations to converge the current iterate before advancing to the next time level[7]:

$$[(\Omega_L/\Delta t_L)I + B_L]\Delta\bar{q}_L^{k+1} = \bar{r}_L^{k,k+1} \tag{8}$$

The modified algorithm is conceptually represented by Eq. (8), identical to Eq. (4) except that subiterations on Δq^k are accommodated. Equation (6) is modified in a similar manner. The superscript $(k, k+1)$ signifies that the latest available iterate on $\bar{q}^n + \Delta q^k$ is utilized in the evaluation of $\bar{r}_L$. In theory, Eq. (8) is iterated on all cells until $\Delta\bar{q}^{k+1} - \Delta\bar{q}^k$ is converged to order Δt^2. In practice, $\bar{q}^{n+1}$ is updated after 10–20 subiterations on $\Delta\bar{q}$. This simplification would be unsatisfactory for a time-accurate simulation but is sufficiently accurate to enable recovery of a steady-state solution as discussed in a later section.

Algorithm Metrics

In most applications with crude initializations, the point-implicit algorithm is more robust and efficient in reducing the residual in the early stages. In fact, the line-implicit algorithm will usually fail (increase the residuals and introduce wild fluctuations) when engaged too early in the relaxation process. However, once the solution begins to converge, indicated by a three order of magnitude decrease in the error norm, the line-implicit algorithm is more efficient in terms of iteration count and CPU time. For example, Figs. 1 and 2 show the convergence history for a benchmark problem, laminar flow over a sphere at $V_\infty = 5$ km/s, $\rho_\infty = 0.001$ kg/m^3, $T_\infty = 200$ K, and $T_w = 500$ K. The convergence history is plotted as a function of CPU time in Fig. 1 for a perfect gas model on a coarse grid of 30×32 starting from a uniform flow. CPU times are on an SGI R10000.

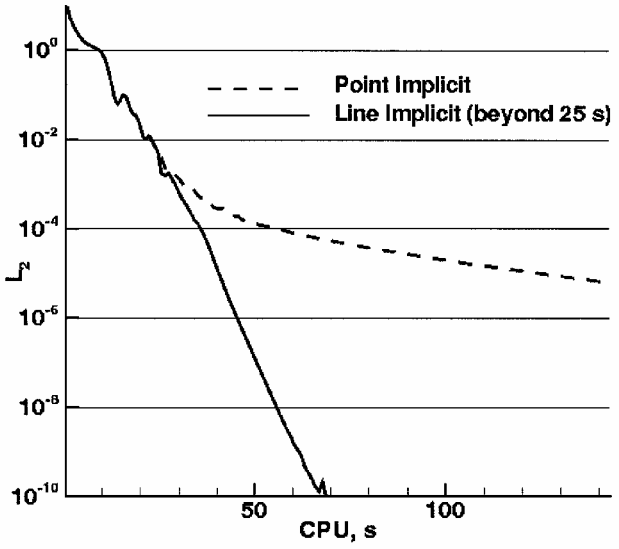

Fig. 1 Comparison of point- and line-implicit CPU time for coarse grid, perfect gas, and sphere benchmark.

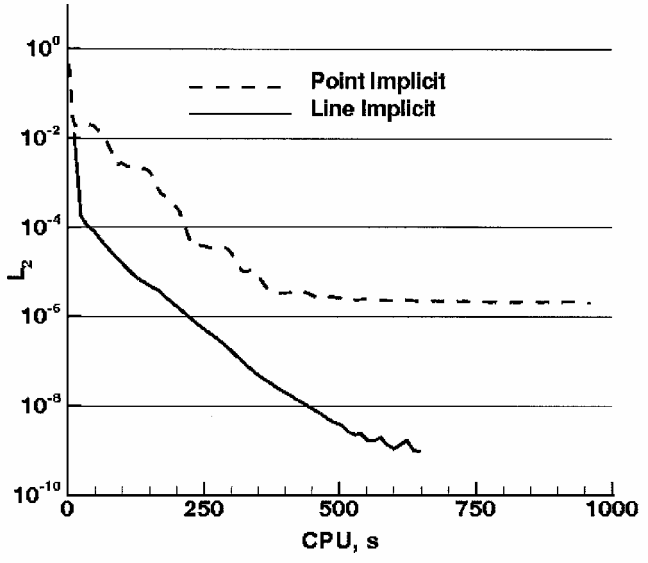

Fig. 2 Comparison of point- and line-implicit CPU time for fine grid, perfect gas, and sphere benchmark.

Subsequent grid refinements initialized from the preceding coarse grid solution to 128 cells in the body-normal direction gives the convergence shown in Fig. 2. The convergence rate slows significantly for the point-implicit case once the inviscid field is nearly converged, but the viscous layer is not fully converged. The line relaxation across the shock layer converges rapidly until roundoff errors inhibit further error norm reduction. Inclusion of thermochemical nonequilibrium source terms in the gas model does not significantly change the character of convergence for the benchmark case on a grid of 30×64 initialized with freestream conditions.

Applications

Ballutes: Spheres and Toroids

Large, inflatable ballutes (balloon parachutes) have been proposed[8,9] as hypersonic decelerators for planetary aerocapture applications. Table 1 defines benchmark conditions for towed spherical and toroidal ballutes. The primary configuration considered here is a towed toroid, in which the flow disturbed by the towing spacecraft passes through the hole of the toroid. The toroid is still impacted by hypersonic flow off the tow cables, which are nearly in a free-molecular flow regime. Interference effects are not included in the present calculations.

The spherical ballute computations were executed on grids with 30 cells (stagnation streamline to 90-deg outflow boundary) and 64 cells (body to inflow boundary ahead of bow shock). Cell Reynolds numbers were of order one at the wall. A grid refinement test for the Neptune orbiter, in which the number of cells were doubled in both directions, showed no change in drag or stagnation point heating through three significant digits. The toroidal ballute simulations used either 60×64 cells for computations over the forebody alone or 120×64 cells for computations including the wake.

Knudsen numbers derived from the mean free path in the freestream to body diameter are of order 0.001–0.01. Knudsen numbers in the boundary layer, relative to boundary-layer thickness, are smaller by a factor of 10. The highest Knudsen number range defines a domain of marginal validity for the Navier–Stokes computations. Continuum simulations tend to be conservative (drag is underpredicted, heating is overpredicted) relative to more accurate particle simulations in this domain. A direct simulation Monte Carlo (DSMC) simulation of rarefied flow for the Titan Organics Explorer spherical ballute from Table 1 predicted $C_D = 1.05$ and $q_{\text{stag}} = 1.76$ W/cm^2. These results are in reasonably good agreement with the continuum results in Table 1. (A simplified gas model including only N_2 and N was assumed.) DSMC simulations appropriate for rarefied and transitional flow must eventually be coupled with continuum analyses to characterize the interactions properly over disparate length scales for towed ballutes. Continuum analyses are appropriate for this initial scoping of the aerothermal loads.

Table 1 Ballute simulations

	Mission				
Parameter	Venus sample return	Mars microsat	Saturn ring observer	Titan organics explorer	Neptune orbiter
Atmosphere, $\chi_{i,\infty}$	$CO_2 = 0.965$ $N_2 = 0.035$	$CO_2 = 0.953$ $N_2 = 0.027$ $Ar = 0.016$ $O_2 = 0.004$	$H_2 = 0.963$ $He = 0.037$	$N_2 = 0.983$ $CH_4 = 0.017$	$H_2 = 0.80$ $He = 0.19$ $CH_4 = 0.001$
Sphere					
D, m	135	12	120	48	100
V_∞, km/s	10.6	5.54	24.1	8.53	26.7
ρ_∞, kg/m^3	2.2×10^{-7}	1×10^{-6}	3.1×10^{-8}	3.0×10^{-7}	1.5×10^{-8}
C_D	0.913	0.99	0.98	0.981	1.05
$\dot{q}_{\max}$, W/cm^2	1.07	1.82	2.72	1.93	2.60
$T_{\max}$, K	677	774	855	785	845
Toroid					
Ring D/cross section D, m	150/30	15/3	120/30	52/13	100/25
V_∞, km/s	10.6	5.49	23.9	8.55	26.8
ρ_∞, kg/m^3	1.6×10^{-7}	7.1×10^{-7}	2.3×10^{-8}	1.9×10^{-7}	8.2×10^{-9}
C_D	1.31	1.45	1.38	1.39	1.51
$\dot{q}_{\max}$, W/cm^2	1.31	1.91	2.85	2.05	2.84
$T_{\max}$, K	712	783	865	796	864

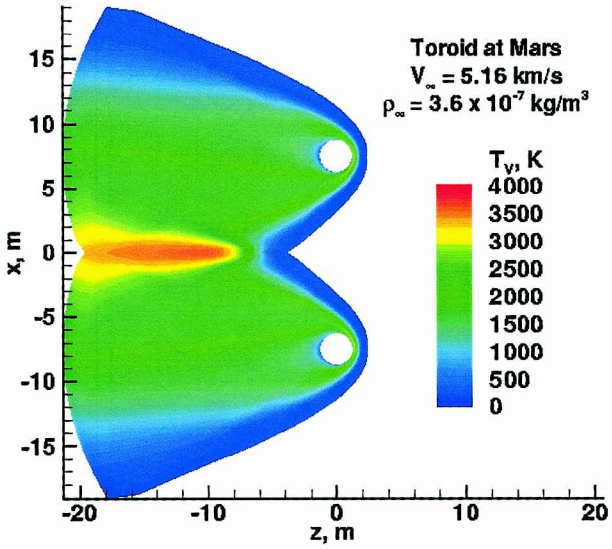

Fig. 3 Vibrational–electronic temperature contours over toroid.

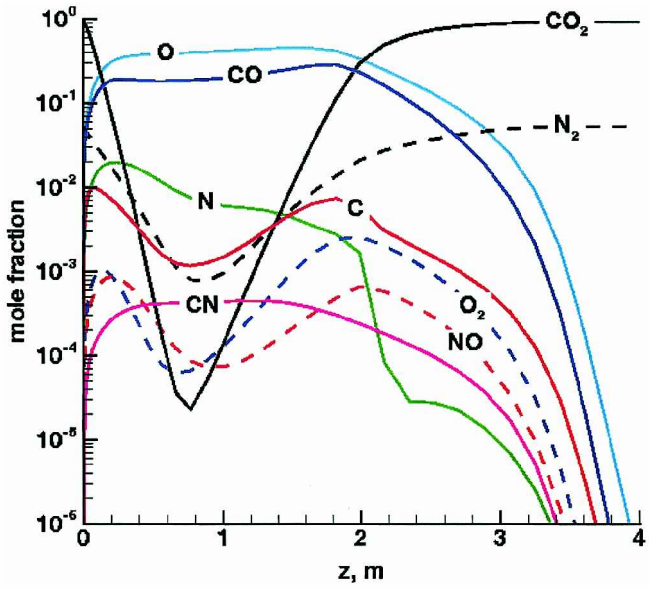

Fig. 4 Mole fraction of neutrals across shock layer of Venus toroid.

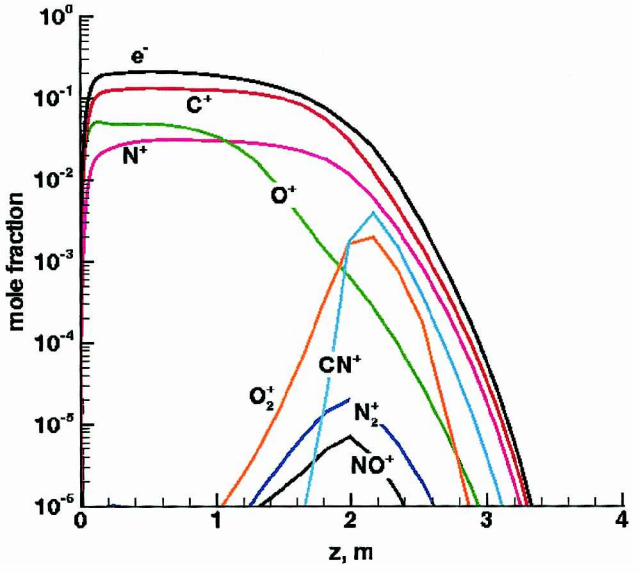

Fig. 5 Mole fractions of ions and electrons across shock layer of Venus toroid.

Physical models in LAURA[10] have been updated to include chemical species expected in the shock layer of ballutes entering the atmospheres of Venus, Saturn, Titan, and Neptune, in addition to the models for Mars and Earth already present. Recently added kinetic models for systems including H_2, He, and CH_4 are taken from papers by Nelson et al.,[11] Nelson,[12] and Liebowitz and Kuo.[13] Thermodynamic curve fits have been updated from the data sets used in the NASA John H. Glenn Research Center at Lewis Field Chemical Equilibrium with Applications Program[14] and by Gordon and McBride.[15] In cases where temperatures fall outside the range of curve fits, the heat capacities are held constant at their respective values at the boundaries of the range; other thermodynamic properties are then computed consistent with this approximation. Collision cross sections $\Omega_{i,j}^{(1,1)}$ and $\Omega_{i,j}^{(2,2)}$ for species i and j at 2000 and 4000 K are derived from data by Kestin and Wakeham[16] and Svehla.[17] Linear fits of $\log(\Omega)$ vs $\log(T)$ are derived from these data. The current model can accommodate 32 species and 57 reaction pairs. Examples for Mars and Venus follow.

The axisymmetric flow past a toroid at Mars for $V_\infty = 5160$ m/s and $\rho_\infty = 3.6 \times 10^{-7}$ kg/m^3 (not part of Table 1) is presented in Fig. 3. The diameter of the toroid, measured from center to center of the circular area of revolution, is 15 m. The cross-sectional diameter of the circle is 2.5 m. Figure 3 shows vibrational–electronic temperatures in a symmetry plane. The computational domain includes the flow axis, coincident with the axis of the toroid; the inflow boundary ahead of the captured bow shock; and the supersonic outflow boundary. The flow is computed with 120 cells around the toroid and 64 cells from the body to the outer boundaries just noted. The near wake is included to investigate the bow-shock interaction along the flow axis and to accommodate future studies of flow interaction from the towing payload passing through the hole. A relatively high-temperature interaction region is evident behind a Mach reflection as the intersecting bow shocks converge on the axis.

The toroid for a Venus Sample Return mission is larger than that required for the Mars Microsat mission noted earlier. It has a more severe entry environment, as detailed in Table 1, but the larger radius reduces heating rate, even with a fully catalytic wall boundary condition. The radiative equilibrium wall temperature at the stagnation point for this case is 712 K. The peak shock-layer vibrational–electronic temperature is approximately 12,000 K.

Profiles of species mole fraction across the shock layer are presented in Figs. 4 and 5. On this scale, body and shock standoff distances on the order of several meters are computed. Significant ionization (20%) is also present. Models for ionization kinetics[11] and simplifications forcing zero conduction current[10] potentially have a large impact on aerothermal loads at these relatively high-ionization levels that are not yet quantified. Note that there is no region of chemical equilibrium; the mole fraction of CO_2, for example, does not begin significant dissociation until about 2 m in front of the body and shows a local minimum with no plateau near the boundary-layer edge. The catalysis model used here forces recombination to freestream levels at the wall; consequently, effects of diffusion and recombination contribute to the rapid increase in CO_2 mole fraction from about 0.7 m to the wall. This case was computed with the line-implicit relaxation algorithm.

Ballutes: Experimental Data

Experimental conditions[18,19] for shot 2018 in the T5 Hypervelocity Shock Tunnel with test gas CO_2, $V_\infty = 3.714$ km/s, $\rho_\infty = 1.61 \times 10^{-3}$ kg/m^3, and $T_\infty = 1570$ K involving flow over a stainless-steel toroid at $\alpha = 0$ deg was simulated with LAURA. Freestream dissociation levels were independently computed[18] to be 0.32, 0.17, 0.42, and 0.09 by mole fraction for CO_2, O_2, CO, and O, respectively. Initial comparisons of the experimental and computational results for convective heating in a CO_2-dominant atmosphere over a ballute are presented in Fig. 6. The effects of uncertainties in boundary conditions on predicted heating levels were not investigated. However, similar quality comparisons were obtained for shots 2013 and 2019, spanning a postshock Reynolds number range from 6.6×10^4 to 2.0×10^5.

Thermal nonequilibrium is assumed and the vibrational–electronic temperature in the freestream is set equal to the

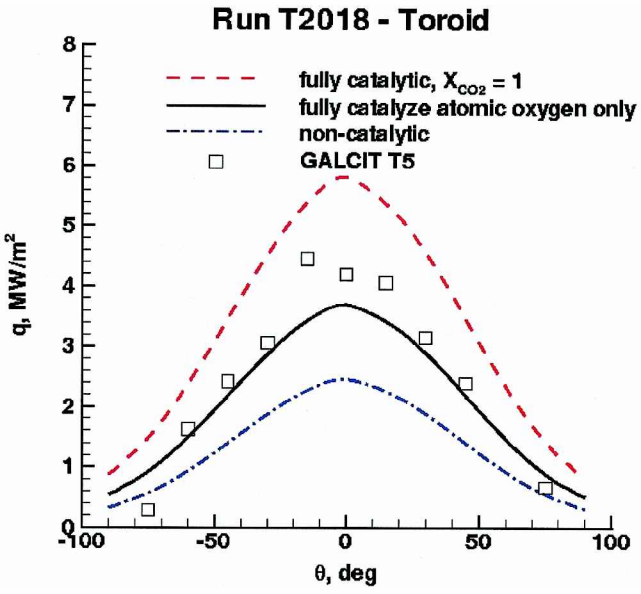

Fig. 6 Heat transfer over toroidal ballute measured in the Graduate Aeronautical Laboratories, California Institute of Technology, T5 hypervelocity shock tunnel in CO_2 and computed by LAURA.

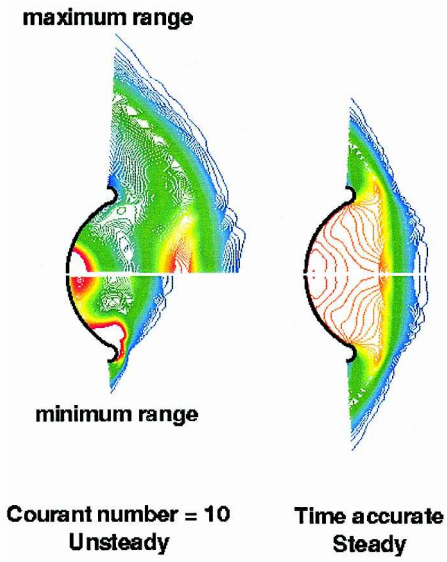

Fig. 7 Density contours over chute at Mach 6 showing unsteady range of motion using constant Courant number simulation and steady solution from time-accurate simulation.

translational–rotational temperature. A constant wall temperature equal to 300 K is specified. Boundary conditions for surface catalysis are varied to scope their influence on heating. In the fully catalytic boundary condition, the mass fraction of CO_2 is set equal to one at the cold wall. Mole fraction gradients are set to zero at the wall for the noncatalytic condition. In an intermediate approximation, it is assumed that atomic oxygen diffusing to the wall recombines to form molecular oxygen, but a zero gradient is employed for all other species. Reasonably good agreement in heating is obtained with the boundary condition in which only oxygen catalysis is accommodated. In all three simulated shots, the experimental data (except near $\theta = 90$ deg) are bounded by the fully catalytic and oxygen-only catalytic curves.

Effects of Time-Accurate Simulation

Disk and parachutelike configurations were also simulated in the early phases of this study, but were not brought forward in Table 1 because of concerns regarding flow stability and aerodynamic stability. The chute configurations failed to converge using the constant Courant number relaxation scheme. Rather, they showed a periodic growth and collapse of the shock wave, the extremes of which are shown in Fig. 7 for a simple Mach 6, perfect gas flow. Instabilities have been reported previously in blunt body flows with cavities.[20] Although the magnitude of these chute instabilities was larger than previously reported, their occurrence was not all that surprising.

The phenomenon was interesting enough to revisit to generate a time-accurate simulation once the capability was developed in LAURA. However, the time-accurate simulation shows that the periodic motion decays to a steady state in approximately eight cycles starting from $t = 0$. The time step was set at 5.23×10^{-6} s. The reference flow time, D/V_∞, is 1.05×10^{-4} s. If the constant Courant number simulation is initiated from a fully converged steady state, the steady state is retained. If the constant Courant number simulation is initiated from a nearly converged time-accurate solution, one that has seen a four-order magnitude drop in error norm, the large-scale periodic motion returns. Use of a constant time step does not, in itself, enable a steady-state solution. In fact, if insufficient subiterations are applied, the unsteady motion is diminished, but will not disappear.[21] Density contours across the shock front in Fig. 7 are somewhat jagged because the grid had to be large enough to fully contain unsteady motion, and grid lines did not align well with the moving shock front.

This unexpected result, in which the ability to achieve a steady state requires temporal accuracy, has not been observed previously in typical, convex blunt-body geometries. However, in a recent hypersonic code validation study,[22] simulated flow over a sharp, double cone (25/55 deg) at Mach 9.5 and Reynolds number 2.64×10^5 m^{-1} in nitrogen showed large-scale, periodic shedding of vortices in the separation region around the 30-deg compression. A first-order accurate, constant Courant number simulation showed a steady flow for this same case. A second-order simulation at a lower Reynolds number (1.44×10^5 m^{-1}) showed a steady flow result on the same grid. Experimental data[23] in the Calspan–University at Buffalo Research Center Large Energy National Shock tunnel for this case (run 24) from thin-film heat transfer gauges indicated that the flow achieved steady state in the test time. The nonlinear minmod flux limiter in LAURA was a suspected source of numerical ringing within the recirculation region that triggered the unsteadiness.

In light of these recent results showing that attainment of a steady state can depend on temporal accuracy in some circumstances, the sharp, double-cone case was revisited using time-accurate simulation. The time step was set at 3.65×10^{-7} s. The reference flow time, L/V_∞, is 7.08×10^{-5} s. The flow converged to a nearly steady state; very slight oscillation of streamlines persisted in the recirculation region, but these oscillations were orders of magnitude less severe than observed in the constant Courant number simulation. Good agreement with the onset of separation and fair agreement with reflected wave peak pressure and heating location are now obtained.

Both the chute and double-cone cases have a subsonic region contained in a concavity (rays perpendicular to the surface converge in a subsonic domain) driven by an external supersonic flow. In the typical grid that is highly stretched from the body, a constant Courant number simulation means that physical time advances more rapidly away from the body than close to the body. Perturbations associated with each relaxation step may tend to aggregate near the wall in the concavity before exiting a supersonic outflow boundary. Waves accumulate (in this nonphysical temporal map), strengthen, and reflect back in to the subsonic domain in a self-sustaining but nonphysical manner. This scenario is consistent with observed behavior in the two systems tested here. Certainly, not all subsonic domains with concavities induce this pseudounsteady behavior in constant Courant number simulations; there are many examples of compression corners with separated flow being computed with constant Courant number relaxation. It is simply noted that such flow conditions may be susceptible to pseudounsteady behavior in single storage level, constant Courant number relaxation, and the overhead associated with implicit, time-accurate simulation may be recovered with better convergence.

Mars Sample Return Orbiter: Flight at Mars

The Mars Sample Return Orbiter (MSRO) is designed to use aeroassist to enter Mars orbit. Though Mars mission architectures

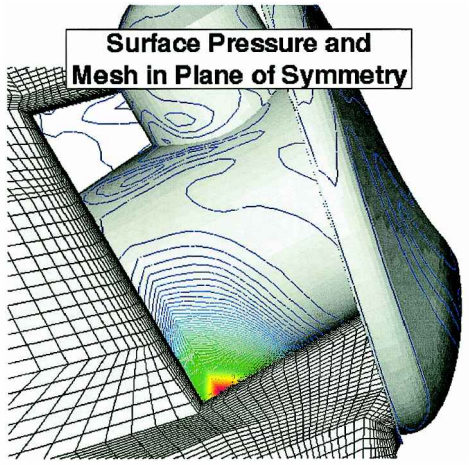

Fig. 8 MSRO near wake mesh and surface pressure distribution.

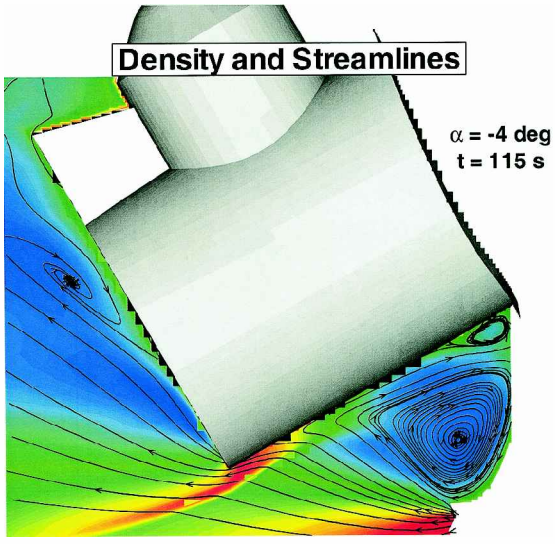

Fig. 9 Density contours and streamlines in symmetry plane featuring primary and secondary vortices behind cove of brake (removed for clarity).

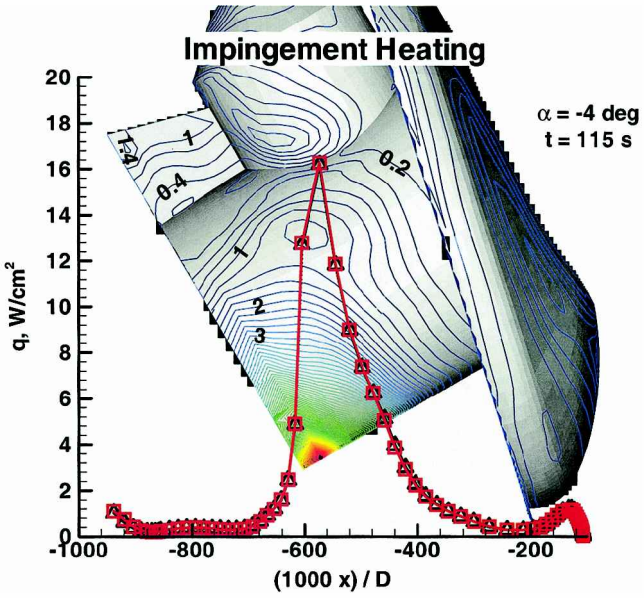

Fig. 10 Trace of heating on symmetry plane of payload showing maximum value at impingement and local maximum under secondary vortex in cove region.

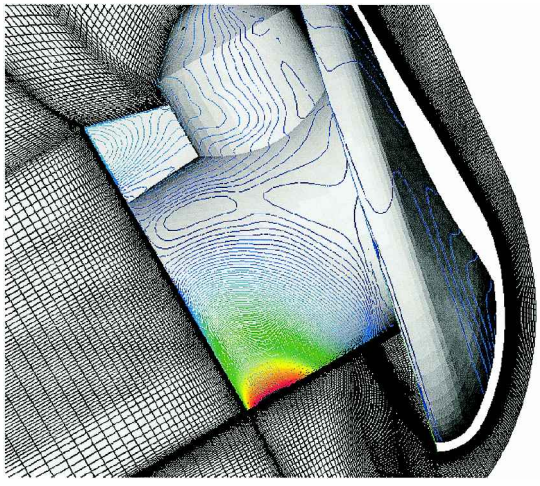

Fig. 11 Grid over MSRO for CF_4 wind-tunnel study with surface pressure distribution.

have been revised, the MSRO mission investigated here called for the French-designed orbiter to carry the U.S.-designed Earth entry vehicle (EEV) to Mars orbit. It would rendezvous with samples gathered in previous missions that had been launched from the surface to orbit. The samples would be sealed in the EEV, which separates from the MSRO and returns to Earth.

One of the concerns in the design is the requirement to protect the payload from impingement heating during the aeropass. Impingement may result from the shear layer separating from the aft edge of the aerobrake and turning significantly inboard. The shear-layer turning angle has been estimated from previous computational and experimental studies[24] of the Aeroassist Flight Experiment vehicle from which MSRO design evolved. An angle of attack α of -4 deg corresponds to a 21-deg angle of attack relative to the base plane. At this relative angle of attack, the shear-layer turning angle should lie between 30 and 40 deg, relative to a backward-facing normal to the base plane. (See Fig. 11 of Ref. 24.) The payload is positioned in a region where shear-layer impingement may be expected on the aft, windside corner. (Payload volume and trim angle-of-attack sensitivity to center of gravity constrain the ability to avoid impingement completely.) Ground-based experimental and computational studies described hereafter confirm shear-layer impingement on the aft corner of the cylindrical payload.

Figures 8–10 show the computed, near-wake results for the MSRO at 115 s into the aeropass at Mars. Flow conditions are $V_\infty = 5223$ m/s and $\rho_\infty = 2.933 \times 10^{-4}$ kg/m^3 at $\alpha = -4$ deg. This angle of attack provides the strongest impingement within the constraints of the guidance system. The computational grid in the plane of symmetry is shown in Fig. 8. There are 434 simply connected, structured blocks used in the near-wake simulation. Inflow conditions were taken from a previously converged forebody solution.

The aerobrake is removed in Fig. 9 to reveal the recirculation region behind the cove. Density contours in Fig. 9 clearly show the shock set up over the aft corner of the payload where impingement occurs. Figure 10 shows a heating trace along the symmetry plane of the payload, superimposed on a global view of surface heating contours. Locally high impingement heating is consistent with observations in ground-based tests. Cell Reynolds number metrics at the wall are of order one or less, so that boundary-layer resolution should be adequate. However, the grid between the aft corner of the aerobrake and the aft corner of the cylinder (Fig. 8) is not well aligned to resolve the free shear layer, so that some numerical diffusion of the flow feeding the impingement is expected.

MSRO: CF_4 Tunnel

Wind-tunnel tests[25] of the MSRO configuration were executed in the NASA Langley Research Center CF_4 tunnel to study impingement heating levels in a gas with a relatively low ratio of specific heat, as will be encountered in flight. The configuration is a scale model of the flight vehicle simulated earlier, but a new grid (Fig. 11)

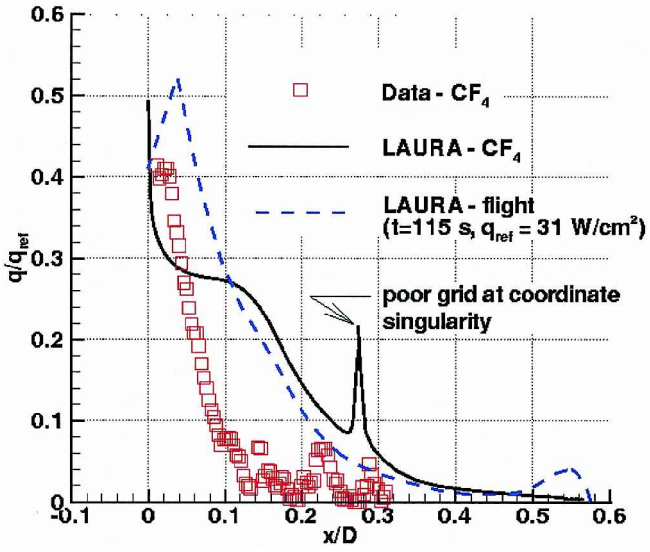

Fig. 12 Impingement zone heating on cylinder along plane of symmetry.

was generated for this study to simplify blocking topology (70 simply connected blocks) and enable automatic grid adaptation into the far field. The new grid has finer resolution in the free shear layer but is still not well aligned with streamlines approaching the aft corner.

Simulated flow conditions are $V_\infty = 907.4$ m/s, $\rho_\infty = 1.53 \times 10^{-3}$ kg/m^3, and $T_\infty = 201.1$ K. Fully laminar flow is expected at this condition based on observed trends in the experiment as a function of Reynolds number.[25] Heating along the leading edge of the cylindrical payload (Fig. 12) is nondimensionalized by a reference stagnation point heating level defined by the method of Fay and Ridell. This reference heating is about 10% larger then measured stagnation point heating for a related case; only a few forebody measurements were made because the study was focused on payload heating issues. Comparisons between experiment (thermophosphor technique) and computation were generally within 8% on the forebody in this related case. The abscissa of Fig. 12 refers to the running length along the cylinder, nondimensionalized by aerobrake reference diameter, originating at the aft corner, and running forward toward the aerobrake.

The experimental data (symbols) indicate a glancing impingement, in which heating is highest at the corner. The LAURA results indicate a stronger impingement, in which a plateau level of heating is predicted, as well as a subsequent heating spike at the corner ($x/D = 0$), where there is a rapid thinning of the boundary layer as flow expands into the wake. A grid refinement (factor two in the streamwise and circumferential directions) provides better resolution of the shear layer, but shows essentially no change (less than 3%) in surface heating. A heating spike near $x/D = 0.3$ is grid induced; four blocks fan out from this location to define the cove region, and the streamwise coordinate of the two central blocks in the fan spans the boundary layer with inadequate resolution.

The flight simulation of heating from Fig. 10 is rescaled and plotted in Fig. 12. In this case, q_{ref} is the computed heating level at the stagnation point on the forebody. At an earlier point in the trajectory ($t = 70$ s, not plotted here) the same trend is observed, but it scales lower, such that the maximum value is $q/q_{ref} = 0.3$. The grid along the cylinder was coarser in the flight case, but did not have a singularity. There is no plateau in heating, possibly because the grid is too coarse to support one. Still, the general trend is that LAURA predicts a larger area of high heating surrounding impingement on the given grids than that measured in CF_4. Additional simulations are planned with realigned grids and, possibly, application of slip-boundary conditions in an attempt to resolve differences in the CF_4 case.

Summary

Point- and line-implicit relaxation algorithms within the program LAURA for aeroassist applications are defined. The strategy of opening with a more robust point-implicit solver and closing with a more aggressive and efficient line relaxation was applied to every problem in this paper. Convergence metrics are documented for a model problem. Implicit wall boundary conditions for the fully coupled, thermochemical nonequilibrium system are required to make the line relaxation strategy work.

Hypersonic flows with subsonic regions bounded by a local concavity were observed to support periodic, unsteady behavior using a constant Courant number relaxation, but a steady flow behavior was recovered using time-accurate simulation. The behavior is thought to emerge from the temporal mapping allowing accumulated perturbations to reflect back into the subsonic domain.

Hypersonic flows over spherical, toroidal, and concave ballute (balloon parachute) decelerators for planetary missions are tested to demonstrate applications with diverse chemical and thermal models in severe environments. Representative environments for entries to Venus, Mars, Saturn, Titan, and Neptune are documented. A parachutelike ballute exhibited the unsteady behavior noted earlier. Comparisons to experimental heating data in T5 for hypersonic flow over a toroid in CO_2 show heating levels bounded by two strongly catalytic models for recombination at the surface.

Simulation of flow over an MSRO adds geometric complexity to the suite of tests. The focus here is on the magnitude of heating on the payload behind an aerobrake caused by impingement of energetic flow expanding around the corner of the aerobrake.

Simulations at a representative flight condition and in a CF_4 tunnel are compared to thermophosphor heating data surrounding the location of shear-layer impingement on the payload. There is a somewhat stronger turning of the shear layer toward the payload in the computational fluid dynamics simulation than is evident in the wind-tunnel data; however, both sources show roughly the same level of peak heating at the aft corner of the payload.

Acknowledgments

J. Oswald of ONERA, in association with the Centre National d'Etudes Spatiales design of the Mars Sample Return Orbiter (MSRO), provided the original computational grid for the flight case. S. Alter of NASA Langley Research Center and D. Nark of Computer Sciences Corporation provided the MSRO grid used in the CF_4 simulation. A. Rasheed of the California Institute of Technology provided early access and commentary to experimental data used here for ballute data in T5. T. Horvath of NASA Langley Research Center provided MSRO data in the CF_4 tunnel. J. Moss and C. Glass of NASA Langley Research Center provided discrete simulation Monte Carlo simulation support.

References

[1]Gnoffo, P. A., "Planetary-Entry Gas Dynamics," *Annual Review of Fluid Mechanics*, Vol. 31, 1999, pp. 459–494.

[2]Gnoffo, P. A., "An Upwind-Biased, Point-Implicit Relaxation Algorithm for Viscous Compressible Perfect Gas Flows," NASA TP 2953, Feb. 1990.

[3]Cheatwood, F. M., and Gnoffo, P. A., "Users Manual for the Langley Aerothermodynamic Upwind Relaxation Algorithm (LAURA)," NASA TM 4674, April 1996.

[4]Roe, P. L., "Approximate Riemann Solvers, Parameter Vectors, and Difference Schemes," *Journal of Computational Physics*, Vol. 43, No. 2, 1981, pp. 357–372.

[5]Harten, A., "High Resolution Schemes for Hypersonic Conservation Laws," *Journal of Computational Physics*, Vol. 49, No. 2, 1983, pp. 357–393.

[6]MacCormack, R. W., "Current Status of the Numerical Solution of the Navier–Stokes Equations," AIAA Paper 85-0032, Jan. 1985.

[7]Mitterer, K. F., Mitcheltree, R. A., and Gnoffo, P. A., "Application of Program LAURA to Perfect Gas Shock Tube Flows—A Parametric Study," NASA TM 104190, Jan. 1992.

[8]Hall, J. L., "A Review of Ballute Technology for Planetary Aerocapture," International Academy of Astronautics, Paper IAA-L-1112, May 2000.

[9]Hall, J. L., and Le, A. K., "Aerocapture Trajectories for Spacecraft with Large Towed Ballutes," American Astronautical Society, Paper AAS 01-235, Feb. 2001.

[10]Gnoffo, P. A., Gupta, R. N., and Shinn, J. L., "Conservation Equations and Physical Models for Hypersonic Air Flows in Thermal and Chemical Nonequilibrium," NASA TP-2867, Feb. 1989.

[11]Nelson, H. F., Park, C., and Whiting, E. E., "Titan Atmospheric Composition by Hypervelocity Shock-Layer Analysis," *Journal of Thermophysics and Heat Transfer*, Vol. 5, No. 2, 1991, pp. 157–165.

[12]Nelson, H. F., "Effect of a Finite Ionization Rate on the Radiative Heating of Outer Planet Atmospheric Entry Probes," NASA CR-3577, June 1982.

[13]Liebowitz, L. P., and Kuo, T.-J., "Ionizational Nonequilibrium Heating During Outer Planetary Entries," *AIAA Journal*, Vol. 14, No. 9, 1976, pp. 1324–1329.

[14]McBride, B. J., and Gordon, S., "Computer Program for Calculation of Complex Chemical Equilibrium Compositions and Applications. II. Users Manual and Program Description," NASA RP 1311, June 1996.

[15]Gordon, S., and McBride, B. J., "Thermodynamic Data to 20,000 K for Monatomic Gases," NASA TP-1999-208523, June 1999.

[16]Kestin, J., and Wakeham, W. A., *Volume I-1 Transport Properties of Fluids Thermal Conductivity, Viscosity, and Diffusion Coefficient*, edited by C. Y. Ho, Cindas Data Series on Material Properties, Hemisphere, New York, 1988, pp. 269–297.

[17]Svehla, R. A., "Estimated Viscosities and Thermal Conductivities of Gases at High Temperatures," NASA TR R-132, 1962.

[18]Rasheed, A., Fujii, K., Valiferdowsi, B., and Hornung, H., "Preliminary Experimental Investigation of the Flow over a Toroidal Ballute," Graduate Aeronautical Labs., California Inst. of Technology, GALCIT Rept. FM 00-4, Pasadena, CA, July 2000.

[19]Rasheed, A., Fujii, K., Hornung, H. G., and Hall, J. L., "Experimental Investigation of the Flow over a Toroidal Aerocapture Ballute," AIAA Paper 2001-2460, June 2001.

[20]Huebner, L. D., and Utreja, L. R., "Mach 10 Bow-Shock Behavior of a Forward-Facing Nose Cavity," *Journal of Spacecraft and Rockets*, Vol. 30, No. 3, 1993, pp. 291–297.

[21]Gnoffo, P. A., "On the Numerical Convergence to Steady State of Hypersonic Flows Over Bodies with Concavities," West East High Speed Flow Field 2002, April 2002.

[22]Gnoffo, P. A., "CFD Validation Studies for Hypersonic Flow Prediction," AIAA Paper 2001-1025, Jan. 2001.

[23]Holden, M. S., and Wadhams, T. P., "Code Validation Study of Laminar Shock/Boundary Layer and Shock/Shock Interactions in Hypersonic Flow Part A: Experimental Measurements," AIAA Paper 2001-1031, Jan. 2001.

[24]Gnoffo, P. A., Price, J. M., and Braun, R. D., "Computation of Near-Wake Aerobrake Flowfields," *Journal of Spacecraft and Rockets*, Vol. 29, No. 2, 1992, pp. 182–189.

[25]Horvath, T. J., Heiner, N. C., Olguin, D. M., Gnoffo, P. A., and Cheatwood, F. M., "Afterbody Heating Characteristics of a Proposed Mars Sample Return Orbiter," AIAA Paper 2001-3068, June 2001.

T. C. Lin
Associate Editor

Color reproductions courtesy of NASA Langley Research Center.